Single-particle EM reveals plasticity of interactions between the adenovirus penton base and integrin $\alpha_V\beta_3$

David Veesler[a], Karolina Cupelli[b], Markus Burger[c], Peter Gräber[c], Thilo Stehle[b,d,1], and John E. Johnson[a,1]

[a]Department of Integrative Structural and Computational Biology, The Scripps Research Institute, La Jolla, CA 92037; [b]Interfaculty Institute of Biochemistry, University of Tuebingen, D-72076 Tuebingen, Germany; [c]Department of Physical Chemistry, University of Freiburg, D-79104 Freiburg, Germany; and [d]Department of Pediatrics, Vanderbilt University School of Medicine, Nashville, TN 37232

Edited by Michael G. Rossmann, Purdue University, West Lafayette, IN, and approved May 2, 2014 (received for review March 11, 2014)

Human adenoviruses are double-stranded DNA viruses responsible for numerous infections, some of which can be fatal. Furthermore, adenoviruses are currently used in clinical trials as vectors for gene therapy applications. Although initial binding of adenoviruses to host attachment receptors has been extensively characterized, the interactions with the entry receptor (integrins) remain poorly understood at the structural level. We characterized the interactions between the adenovirus 9 penton base subunit and $\alpha_V\beta_3$ integrin using fluorescence correlation spectroscopy and single-particle electron microscopy to understand the mechanisms underlying virus internalization and infection. Our results indicate that the penton base subunit can bind integrins with high affinity and in several different orientations. These outcomes correlate with the requirement of the pentameric penton base to simultaneously bind several integrins to enable their clustering and promote virus entry into the host cell.

Human adenoviruses are classified into more than 60 different serotypes and are associated with acute respiratory, gastrointestinal, and ocular infections, as well as fulminant infections among children and immunocompromised patients. Replication-defective or conditionally replicating human adenoviruses are also used in a large number of clinical trials for vaccine and therapeutic gene transfer (1). Adenoviruses are large, nonenveloped double-stranded DNA virions sharing a common capsid architecture based on $T = 25$ icosahedral symmetry (2–4). The hexon, penton base, and fiber proteins are the main capsid building blocks, with several cement proteins further contributing to capsid stability. The structural conservation of hexon- and penton-like proteins among several virus families infecting organisms of the three domains of life suggested that these virions are evolutionarily related and resulted in their classification in the PRD1-adenovirus lineage (2, 3, 5–11).

The trimeric fiber protein and the pentameric penton base are the major players in adenovirus attachment and cell entry. Initial attachment of the virus occurs through the binding of the fiber C-terminal distal knob domain to attachment receptors such as coxsackie and adenovirus receptor (CAR), the complement receptor CD46, the GD1a glycan, or desmoglein-2 (DSG-2) (12). After initial cell attachment, a highly conserved arginine glycine aspartic acid (RGD) motif in a long loop of the penton base subunits engages $\alpha_v\beta_3$ or $\alpha_v\beta_5$ integrins, which serve as entry receptors. Binding to integrins promotes integrin clustering and in turn rapid receptor-mediated internalization of the virion (13). Partially disassembled capsids escape from the endosome and are transported along microtubules to the perinuclear envelope, where further disintegration of the capsid allows import of the viral genome into the nucleus (14).

Although binding of the adenovirus trimeric fiber protein to the attachment receptors CAR, CD46, and GD1a has been extensively characterized, the interactions between the penton base and heterodimeric integrin remain less well understood at the structural level. Integrins are heterodimeric cell-surface transmembrane proteins involved in the regulation of adhesion, migration, growth, and differentiation (15). They form a stalk-like structure composed of a large "headpiece" that engages ligands and slender "legs" that anchor the heterodimer into the membrane. Integrins can assume a bent, inactive conformation, in which the legs are wrapped around the headpiece, as well as more extended, active conformations (16–18). The large multidomain extracellular moiety formed by the two integrin chains is able to bind a variety of ligands, including several viruses (e.g., adenoviruses), whereas the smaller intracellular domains interact with cytoskeletal proteins to carry out bidirectional signaling (19–23). Some integrins, such as $\alpha_v\beta_3$, are able to engage RGD sequences, which are found in various physiological ligands, and a crystal structure of a complex between $\alpha_v\beta_3$ integrin and a small peptide harboring this sequence has shown that the RGD motif binds to an exposed region in the headpiece (17). Located at the interface of the α_v and β_3 chains, the RGD sequence inserts into a cleft formed by the β-propeller domain of the α_v chain and the βA domain of the β_3 chain. All three amino acids—RGD—make specific contacts with headpiece residues. Previous studies have attempted to characterize the interactions between adenovirus and integrin using electron cryo-microscopy and biophysical techniques (24, 25). The results suggested that four integrins could simultaneously bind onto one penton base with varying orientations (due to steric hindrance). However, these interactions could not be analyzed in detail due to the large conformational flexibility of the integrin as well as the symmetry mismatch between the two partners.

Significance

Human adenoviruses are responsible for numerous infections and are used in clinical trials for gene therapy applications. We characterized the interactions between the adenovirus 9 penton base subunit and the entry receptor $\alpha_V\beta_3$ integrin using fluorescence correlation spectroscopy and single-particle electron microscopy to decipher the mechanisms underlying virus internalization and infection. Our results indicate that the penton base subunit can bind integrins with high affinity and, in several different orientations, in agreement with the requirement of the pentameric penton base to promote integrin clustering and virus entry into the host cell.

Author contributions: D.V., K.C., M.B., P.G., T.S., and J.E.J. designed research; D.V., K.C., M.B., and P.G. performed research; D.V., K.C., M.B., P.G., T.S., and J.E.J. analyzed data; and D.V. wrote the paper.

The authors declare no conflict of interest.

This article is a PNAS Direct Submission.

Data Deposition: The reconstructions have been deposited to the Electron Microscopy Data Bank, www.ebi.ac.uk/pdbe/emdb/ (EMDB codes EMD-5955–EMD-5973).

[1]To whom correspondence may be addressed. E-mail: thilo.stehle@uni-tuebingen.de or jackj@scripps.edu.

This article contains supporting information online at www.pnas.org/lookup/suppl/doi:10.1073/pnas.1404575111/-/DCSupplemental.

We set out to describe the interactions between the adenovirus penton base and integrin to understand the mechanisms underlying virus internalization and infection. Our approach differs from previous studies as we used a "minimalist" system, which is composed of the monomeric RGD loop-containing insertion domain of the adenovirus 9 penton base subunit (pb9) and the extracellular region of the $\alpha_V\beta_3$ integrin. The adenovirus 9 serotype was chosen because the penton loop harboring the RGD sequence is among the shortest, and perhaps least flexible, in the adenovirus family. We characterized the binding affinity between $\alpha_V\beta_3$ integrin and pb9 using fluorescence correlation spectroscopy (FCS) and demonstrated that the complex has a dissociation constant in the nanomolar range. We also analyzed the extracellular region of the $\alpha_V\beta_3$ integrin, either unliganded or in complex with the penton base domain, using single-particle electron microscopy. The results unexpectedly indicate that the penton base can bind integrins in several orientations and suggest a putative mechanism for integrin clustering and virion internalization at the onset of infection.

Results

Extracellular Region of $\alpha_V\beta_3$ Integrin Forms a Stable Complex with pb9. Using insect cell expression, we produced a secreted $\alpha_V\beta_3$ construct containing the extracellular domains of the two integrin chains along with the Fos or Jun dimerization domain and a hexahistidine or Strep-tag fused to the C termini of the α- and β-subunits, respectively (Fig. S1*A*). After affinity purification, we removed the Fos/Jun domains and the tags by HRV3C protease cleavage to yield the soluble, heterodimeric $\alpha_V\beta_3$ ectodomain (Fig. S1*B*). This protein was then further purified by size-exclusion chromatography, either directly or after incubation with an excess of pb9. pb9 comprises the most surface-exposed region of the penton base subunit (amino acids residue 116–360), including the extended loop harboring the RGD motif. As pb9 lacks the base region of the penton base, it can be expressed in *Escherichia coli* and purified as a monomer (Fig. 1*A*). The elution profile of the unliganded integrin featured a single, symmetrical peak indicating the presence of a monodisperse and homogenous sample (Fig. 1*B*). The sample containing pb9 was characterized by the presence of two well-separated peaks with shorter and longer retention times compared with $\alpha_V\beta_3$. We interpreted the first peak as being the complex between the penton base and $\alpha_V\beta_3$ whereas the second peak corresponded to the excess of penton base, as confirmed by SDS/PAGE (Fig. 1 *B* and *C*).

pb9 Binds with Nanomolar Affinity to $\alpha_V\beta_3$ Integrin. We next characterized the affinity between pb9 and $\alpha_V\beta_3$ using FCS. Labeling of the penton base was achieved by thiol coupling of the fluorescent dye Atto532-maleimide with the residue Cys-208, which is distal to the RGD motif. Diffusion times (τ_D) of pb9 alone and in the presence of various concentrations of $\alpha_V\beta_3$ integrin were measured in a confocal setup. Saturation in the diffusion time was reached at an integrin concentration of 2.45 μM. The influence of added integrin on the diffusion time of the labeled pb9 was used to analyze the binding affinity (Fig. 2*A*). We determined a dissociation constant (K_D) of 415 ± 62 nM for the complex by extrapolating the concentration of added $\alpha_V\beta_3$ required to bind to 50% of the penton base in solution (Fig. 2*B*). These results demonstrated that the penton base construct that we used bound with high affinity to $\alpha_V\beta_3$ integrin and was suitable for structural studies.

Structure of $\alpha_V\beta_3$ Integrin in the Absence of Ligand. Structural analyses of $\alpha_V\beta_3$ had shown that the heterodimer can assume a bent, inactive conformation in which the "legs" are wrapped around the headpiece, as well as a range of more extended conformations that represent different stages of activation (18). These

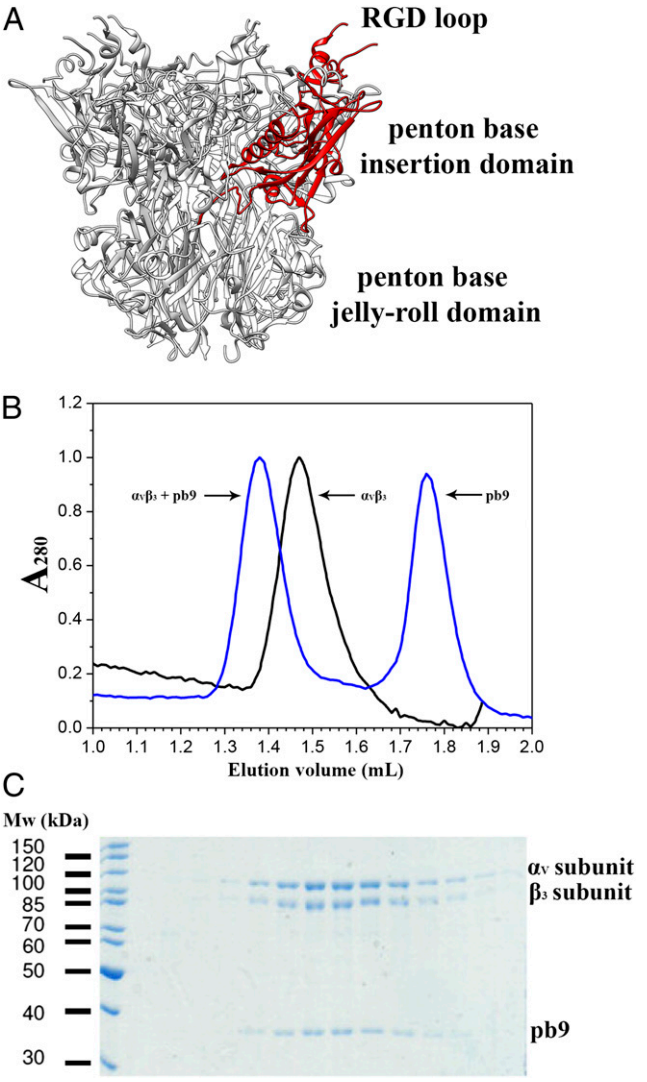

Fig. 1. Purification of the $\alpha_V\beta_3$ integrin–pb9 complex. (*A*) Ribbon representation of the adenovirus 2 penton base pentamer [Protein Data Bank (PDB) ID 1 × 9P]. Four out of the five monomers are colored grey, while the fifth one has its base domain colored white and its insertion domain colored red (the latter region corresponds to the construct used in this study). (*B*) Size-exclusion chromatography elution profiles of $\alpha_V\beta_3$ integrin alone [in the presence of 2 mM $MgCl_2$ (black curve)] or in complex with pb9 [in the presence of 2 mM $MnCl_2$ (blue curve)]. The column used was a Superose 6 PC 3.2/30. (*C*) SDS/PAGE analysis of the complex shown in *B*.

compact and extended forms were visible in our single-particle, negative-stain electron microscopy images of purified integrins, distinguishable as horseshoe-shaped and highly flexible molecules (Fig. S2). To deal with this high degree of heterogeneity, an iterative strategy was used to identify homogeneous classes corresponding to various conformational snapshots of the $\alpha_V\beta_3$ integrin. We identified several different characteristic conformations resulting from the pronounced flexibility of the "leg" domains belonging to chains α_V and β_3 (Fig. 3*A* and Movie S1): (*i*) bent, (*ii*) extended with closed headpiece, and (*iii*) extended with open headpiece. A similar classification was used earlier by Springer et al. (18) to link the existing conformations to different functional states. The high quality of the class averages obtained allowed a straightforward discrimination of the two chains of the $\alpha_V\beta_3$ heterodimer due to the typical triangular shape of the region formed by the propeller domain of the α_V chain and the

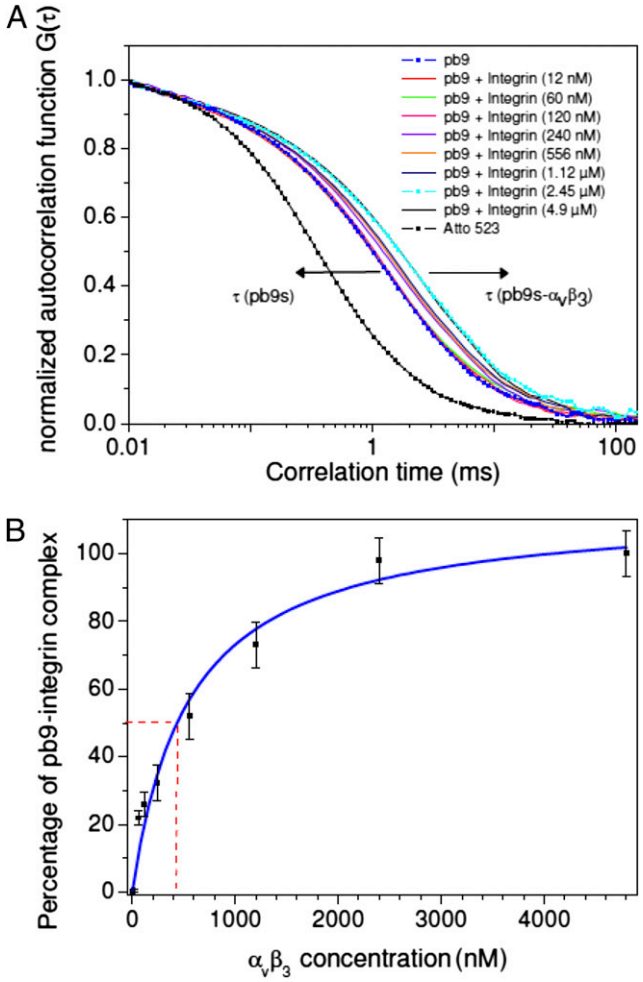

Fig. 2. Characterization of the affinity of the complex formed between $\alpha_V\beta_3$ integrin and pb9 by fluorescence correlation spectroscopy in the presence of 2 mM $MgCl_2$. (*A*) Auto-correlation function of fluorescently labeled pb9 incubated with increasing concentration of $\alpha_V\beta_3$ integrin. (*B*) The proportion of complex formed as a function of the concentration of $\alpha_V\beta_3$ integrin was derived from the correlation times shown in *A*. The equilibrium dissociation constant (K_D) was estimated as 415 ± 62 nM by nonlinear regression analysis.

βA domain of the β-chain. The assignment was further validated by our ability to resolve the density belonging to three consecutive domains forming the α_V chain leg, i.e., thigh, calf-1, and calf-2 (Fig. 3*A*).

We used the random-conical tilt (RCT) approach (26) to compute 3D reconstructions from each independent 2D class average. The resulting density maps feature the expected integrin domains and confirm the presence of several conformational snapshots of the $\alpha_V\beta_3$ integrin (Fig. 3 *B* and *C*). Bent integrins exhibit a characteristic "V" shape due to the folding of the elongated heterodimer onto itself as a result of the interactions formed between the headpiece and tailpiece, similar to what was seen in the crystal structure of inactive $\alpha_V\beta_3$ (16). We also obtained reconstructions corresponding to several extended integrin conformations with various degrees of opening of the α_V and β_3 legs ranging from "crossed" to "wide open" (Movie S1). These conformers can be readily assigned to the known functional states of the integrin life cycle (18, 22, 23), therefore confirming the integrity of the protein after grid preparation.

Plasticity of Interactions Between pb9 and $\alpha_V\beta_3$ Integrin. When pb9 was added to the integrin preparation, an additional density with a roughly globular shape appeared to contact the distal part of the $\alpha_V\beta_3$ headpiece, as observed by negative-stain electron microscopy (Fig. S3). This density could be directly attributed to the penton base insertion domain that is known to bind via its RGD-binding loop to heterodimeric $\alpha_V\beta_3$ integrin, thereby promoting endocytosis of the virion at the onset of infection. Complex formation did not require the integrin molecules to be in a defined conformation as the penton base could bind to both bent and extended integrins and to virtually all possible extended conformational states of the $\alpha_V\beta_3$ legs (Fig. 4 *A* and *B* and Movie S2). We detected at least four different binding modes of pb9 on the integrin headpiece, and these appear to be compatible with the conformational states that the extended integrins can adopt (18), as we obtained snapshots corresponding to all possible combinations.

We again relied on the RCT approach to compute 3D reconstructions of each conformation of the complex. The resulting maps are in good agreement with the corresponding 2D class averages from which they originated, and they support the observation that the penton base insertion domain binds to the $\alpha_V\beta_3$ headpiece at several locations (Fig. 4*C*). These binding modes are profoundly different from each other and correspond to a variation of the penton base position relative to the β-propeller/βA domains of the α_V/β_3 chains (Fig. 5). Indeed, the adenovirus protein is bound at discrete locations between the apex of the integrin headpiece (at the interface between the propeller domain

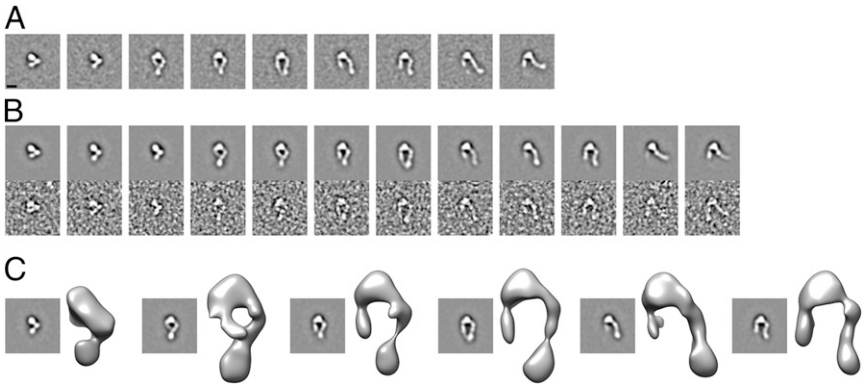

Fig. 3. Single-particle EM analysis of isolated $\alpha_V\beta_3$ integrin in the presence of 2 mM Mn^{2+}. (*A*) Initial reference-free class averages obtained using the iterative stable alignment and clustering program. (*B*) Reference-based class averages used to compute random conical tilt 3D reconstructions. A particle belonging to each class average is shown below the corresponding class. (*C*) Random conical tilt 3D reconstructions showing various integrin conformational states. (Scale bar corresponds to 83 Å and applies to the class averages in *A*–*C*.)

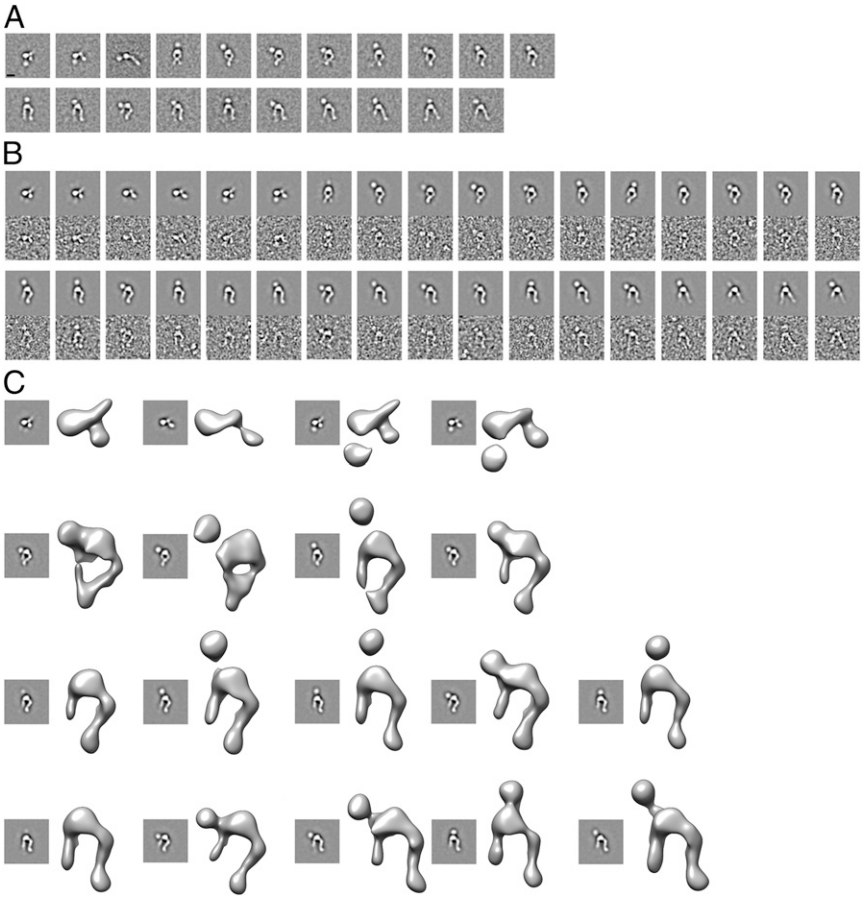

Fig. 4. Single-particle EM analysis of the $\alpha_V\beta_3$ integrin–pb9 complex in the presence of 2 mM Mn^{2+}. (*A*) Initial reference-free class averages obtained using the iterative stable alignment and clustering program. (*B*) Reference-based class averages used to compute random conical tilt 3D reconstructions. A particle belonging to each class average is shown below the corresponding class. (*C*) Random conical tilt 3D reconstructions showing various integrin conformational states and penton base binding modes. (Scale bar corresponds to 97 Å and applies to the class averages in *A*–*C*.)

of the α_V chain and the βA domain of the β_3 chain) and its lateral moiety (at the interface between the βA domain and the hybrid domain of the β_3 chain).

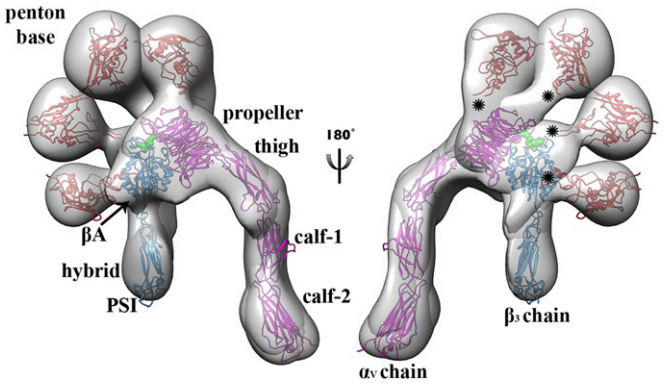

Fig. 5. Plasticity of the $\alpha_V\beta_3$ integrin–pb9 complex. Superimposition of four random conical tilt 3D reconstructions of the complex revealing pb9 (red) bound at various locations onto the integrin headpiece (blue and magenta). The RGD peptide is depicted as green spheres. (*Right*) The black stars indicate the position of the anchor of the RGD loop onto the penton base in each reconstruction. An open model of $\alpha_V\beta_3$ integrin bound to RGD (derived from PDB ID 4G1M) and a model of pb9 (derived from PDB ID 1X9P) are fitted into the RCT reconstructions.

Discussion

Although integrins serve as entry receptors for many viruses (27–30), the molecular details underlying these interactions are not well understood for any virus. The observation that the penton base insertion domain can bind to $\alpha_V\beta_3$ integrin in various different orientations constitutes an unexpected finding, particularly compared with other structural analyses of attachment and entry receptor complexes of viruses. These structures generally depict one state of binding and do not offer insights into possible dynamic aspects of the interaction. Although the interacting partners might be sterically more restrained in vivo, because of quaternary interactions at the penton and icosahedral symmetry of the particle, their relative positions and orientations appear compatible with the presence of the assembled virion. The pb9 RGD loop comprises ~32 residues and can project at most ~55 Å from the penton fold when considering fully extended residues. As we know the exact location of the RGD-binding site on the integrin headpiece (17), we can evaluate the relevance of the different interaction types by measuring the distance between the anchor of the RGD loop onto the penton base and the RGD peptide. All of the binding modes detected by single-particle EM are consistent with the number of residues present in the pb9 RGD loop. The fact that we observed the penton base bound to the $\alpha_V\beta_3$ headpiece region formed by the propeller domain of the α_V chain and the βA domain of the β-chain further supports the biological significance of these various types of interactions.

We were not able to demonstrate any correlation between the penton base binding mode and the conformation of the integrin heterodimer. This outcome can be interpreted either as a result of the versatility of the adenovirus penton base to bind to all possible integrin conformational states or as a consequence of the absence of the $\alpha_V\beta_3$ transmembrane domains that would further restrict the degrees of freedom of the two integrin chains. The observation of the penton base bound to the bent integrin conformation is reminiscent of the situation reported for the complex between integrin $\alpha_V\beta_3$ and fibronectin (19) although the presence of the complete virion might prevent such interactions in vivo due to steric hindrance. Nevertheless, it seems clear that multiple binding modes exist between pb9 and $\alpha_V\beta_3$ and that the complex may form successively and perhaps cooperatively. It is likely that initial interactions involve docking of the RGD sequence into the cleft of $\alpha_V\beta_3$, tethering the virus to the cell surface. The inherent flexibility of the RGD loop could be used by adenoviruses to scan the cell surface, and the different RGD loop/$\alpha_V\beta_3$-binding modes would maximize the likelihood of productive binding. This mechanism might also be the basis of enabling simultaneous accommodation of several integrins with varying orientations onto a single penton base pentamer [as previously suggested (24, 25)] to facilitate their clustering and thus virus internalization. It may be significant that our results are in agreement with what was reported for the coxsackievirus–A9/$\alpha_V\beta_6$ integrin interaction, where surface plasmon resonance data could be fitted with a model involving multiple binding sites (31). It is therefore conceivable that many viruses have evolved the capacity to simultaneously bind to integrin receptors/coreceptors in several distinct ways as a means of promoting cell entry.

Materials and Methods

Fluorescence Correlation Spectroscopy Measurements. Single-molecule fluorescence spectroscopy measurements were performed at room temperature using a home-built confocal microscope setup (32) and a Nd:YAG laser (532 nm, Coherent). Mean diffusion times (τ_D) through the confocal detection volume of ~7 fl were measured by fluorescence correlation spectroscopy by recording the autocorrelation signal for 120 s.

EM Data Collection and Processing. All samples were negatively stained using 2% uranyl-formate. Data were acquired using the Leginon software system (33, 34) and processed using the Appion software package (35, 36), which interfaces with the Leginon database infrastructure. Particle images were clustered in 15 (unliganded $\alpha_V\beta_3$) and 40 ($\alpha_V\beta_3$ in complex with pb9) different class averages, and random conical tilt reconstructions (26) were computed for all of them using the initial model pipeline within the Appion architecture. Fitting of the atomic model within the reconstructions was achieved using University of California at San Francisco Chimera (37) and Coot (38).

ACKNOWLEDGMENTS. We thank Nicolas Binder and Alexandra Thor for assistance with $\alpha_V\beta_3$ expression and Timm Hassemer for assistance with the protein purification of integrin $\alpha_V\beta_3$. We acknowledge funding from a FP7 Marie-Curie International Outgoing Fellowship (273427, to D.V.) and National Institutes of Health (NIH) Grant GM054076 (to J.E.J.). Part of this research was conducted at the National Resource for Automated Molecular Microscopy, which is supported by the NIH and the National Institute of General Medical Sciences (GM103310).

1. Henry TD, et al. (2007) Effects of Ad5FGF-4 in patients with angina: An analysis of pooled data from the AGENT-3 and AGENT-4 trials. *J Am Coll Cardiol* 50(11):1038–1046.
2. Liu H, et al. (2010) Atomic structure of human adenovirus by cryo-EM reveals interactions among protein networks. *Science* 329(5995):1038–1043.
3. Reddy VS, Natchiar SK, Stewart PL, Nemerow GR (2010) Crystal structure of human adenovirus at 3.5 A resolution. *Science* 329(5995):1071–1075.
4. Stewart PL, Burnett RM, Cyrklaff M, Fuller SD (1991) Image reconstruction reveals the complex molecular organization of adenovirus. *Cell* 67(1):145–154.
5. Veesler D, et al. (2013) Atomic structure of the 75 MDa extremophile Sulfolobus turreted icosahedral virus determined by CryoEM and X-ray crystallography. *Proc Natl Acad Sci USA* 110(14):5504–5509.
6. Khayat R, et al. (2005) Structure of an archaeal virus capsid protein reveals a common ancestry to eukaryotic and bacterial viruses. *Proc Natl Acad Sci USA* 102(52): 18944–18949.
7. Abrescia NG, et al. (2004) Insights into assembly from structural analysis of bacteriophage PRD1. *Nature* 432(7013):68–74.
8. Cockburn JJ, et al. (2004) Membrane structure and interactions with protein and DNA in bacteriophage PRD1. *Nature* 432(7013):122–125.
9. Zubieta C, Schoehn G, Chroboczek J, Cusack S (2005) The structure of the human adenovirus 2 penton. *Mol Cell* 17(1):121–135.
10. Abrescia NG, et al. (2008) Insights into virus evolution and membrane biogenesis from the structure of the marine lipid-containing bacteriophage PM2. *Mol Cell* 31(5): 749–761.
11. Roberts MM, White JL, Grütter MG, Burnett RM (1986) Three-dimensional structure of the adenovirus major coat protein hexon. *Science* 232(4754):1148–1151.
12. Cupelli K, Stehle T (2011) Viral attachment strategies: The many faces of adenoviruses. *Curr Opin Virol* 1(2):84–91.
13. Wickham TJ, Mathias P, Cheresh DA, Nemerow GR (1993) Integrins alpha v beta 3 and alpha v beta 5 promote adenovirus internalization but not virus attachment. *Cell* 73(2):309–319.
14. Nemerow GR, Stewart PL (1999) Role of alpha(v) integrins in adenovirus cell entry and gene delivery. *Microbiol Mol Biol Rev* 63(3):725–734.
15. Arnaout MA, Mahalingam B, Xiong JP (2005) Integrin structure, allostery, and bidirectional signaling. *Annu Rev Cell Dev Biol* 21:381–410.
16. Xiong JP, et al. (2001) Crystal structure of the extracellular segment of integrin alpha Vbeta3. *Science* 294(5541):339–345.
17. Xiong JP, et al. (2002) Crystal structure of the extracellular segment of integrin alpha Vbeta3 in complex with an Arg-Gly-Asp ligand. *Science* 296(5565):151–155.
18. Takagi J, Petre BM, Walz T, Springer TA (2002) Global conformational rearrangements in integrin extracellular domains in outside-in and inside-out signaling. *Cell* 110(5):599–511.
19. Adair BD, et al. (2005) Three-dimensional EM structure of the ectodomain of integrin alphaVbeta3 in a complex with fibronectin. *J Cell Biol* 168(7):1109–1118.
20. Takagi J, Strokovich K, Springer TA, Walz T (2003) Structure of integrin alpha5beta1 in complex with fibronectin. *EMBO J* 22(18):4607–4615.
21. Shi M, et al. (2011) Latent TGF-β structure and activation. *Nature* 474(7351):343–349.
22. Zhu J, et al. (2008) Structure of a complete integrin ectodomain in a physiologic resting state and activation and deactivation by applied forces. *Mol Cell* 32(6): 849–861.
23. Chen X, et al. (2010) Requirement of open headpiece conformation for activation of leukocyte integrin alphaXbeta2. *Proc Natl Acad Sci USA* 107(33):14727–14732.
24. Chiu CY, Mathias P, Nemerow GR, Stewart PL (1999) Structure of adenovirus complexed with its internalization receptor, alphavbeta5 integrin. *J Virol* 73(8):6759–6768.
25. Lindert S, Silvestry M, Mullen TM, Nemerow GR, Stewart PL (2009) Cryo-electron microscopy structure of an adenovirus-integrin complex indicates conformational changes in both penton base and integrin. *J Virol* 83(22):11491–11501.
26. Radermacher M (1988) Three-dimensional reconstruction of single particles from random and nonrandom tilt series. *J Electron Microsc Tech* 9(4):359–394.
27. Seitsonen J, et al. (2010) Interaction of alphaVbeta3 and alphaVbeta6 integrins with human parechovirus 1. *J Virol* 84(17):8509–8519.
28. Heikkilä O, Susi P, Stanway G, Hyypiä T (2009) Integrin alphaVbeta6 is a high-affinity receptor for coxsackievirus A9. *J Gen Virol* 90(Pt 1):197–204.
29. Dicara D, et al. (2008) Foot-and-mouth disease virus forms a highly stable, EDTA-resistant complex with its principal receptor, integrin alphavbeta6: Implications for infectiousness. *J Virol* 82(3):1537–1546.
30. Stewart PL, Nemerow GR (2007) Cell integrins: Commonly used receptors for diverse viral pathogens. *Trends Microbiol* 15(11):500–507.
31. Shakeel S, et al. (2013) Structural and functional analysis of coxsackievirus A9 integrin αvβ6 binding and uncoating. *J Virol* 87(7):3943–3951.
32. Börsch M, Diez M, Zimmermann B, Reuter R, Gräber P (2002) Stepwise rotation of the gamma-subunit of EF(0)F(1)-ATP synthase observed by intramolecular single-molecule fluorescence resonance energy transfer. *FEBS Lett* 527(1-3):147–152.
33. Suloway C, et al. (2005) Automated molecular microscopy: The new Leginon system. *J Struct Biol* 151(1):41–60.
34. Yoshioka C, et al. (2007) Automation of random conical tilt and orthogonal tilt data collection using feature-based correlation. *J Struct Biol* 159(3):335–346.
35. Lander GC, et al. (2009) Appion: An integrated, database-driven pipeline to facilitate EM image processing. *J Struct Biol* 166(1):95–102.
36. Voss NR, Yoshioka CK, Radermacher M, Potter CS, Carragher B (2009) DoG Picker and TiltPicker: Software tools to facilitate particle selection in single particle electron microscopy. *J Struct Biol* 166(2):205–213.
37. Pettersen EF, et al. (2004) UCSF Chimera: A visualization system for exploratory research and analysis. *J Comput Chem* 25(13):1605–1612.
38. Emsley P, Lohkamp B, Scott WG, Cowtan K (2010) Features and development of Coot. *Acta Crystallogr D Biol Crystallogr* 66(Pt 4):486–501.

Supporting Information

Veesler et al. 10.1073/pnas.1404575111

SI Materials and Methods

Protein Expression and Purification. *Human adenovirus 9 penton base.* DNA coding for amino acids 116–360 of human adenovirus 9 penton base was cloned into the pET15b expression vector (Novagen) with an N-terminal hexahistidine tag (His-tag) and a HRV3C cleavage site. The protein was overexpressed in *Escherichia coli* Rosetta 2(DE3) and purified by nickel affinity chromatography and size-exclusion chromatography using a Superdex-75. The tag was cleaved with HRV3C protease before the size-exclusion chromatography step.

Integrin $\alpha_V\beta_3$. The extracellular domains of α_V and β_3 were generated as codon-optimized constructs by gene synthesis (GeneArt Gene Synthesis). α_V (amino acids 1–987) was synthesized with a C-terminal HRV3C-cleavage site, followed by a Jun coiled-coil domain and a C-terminal hexahistidine tag (Fig. S1). The extracellular domain of β_3 (amino acids 1–718) was synthesized with a C-terminal HRV3C-cleavage site, followed by a Fos coiled-coil domain and a C-terminal Strep-tag (Fig. S1). The subunits were cloned into the pFastBacDual vector (Invitrogen). $\alpha_V\beta_3$ was expressed in Sf9 cells as a secreted protein by using the baculovirus vector expression system (multiplicity of infection: 0.2; harvest at 72–96 hours postinfection). The supernatant was centrifuged to remove cells (15 min at 500 × *g*). Subsequently, the supernatant was filtrated through a 0.45-μm filter. Concentration of the supernatant and the subsequent buffer exchange to 2 mM $MnCl_2$, 125 mM NaCl, and 25 mM Tris base (pH 8.0) were carried out by tangential flow filtration using a 100-kDa cutoff. The protein was purified by nickel affinity chromatography, followed by a Strep-tag affinity chromatography, proteolytic cleavage by HRV3C, and size-exclusion chromatography using a Superdex 200 column.

Penton Base Labeling and Fluorescence Correlation Spectroscopy Measurements. Labeling of the penton base was achieved by thiol coupling of the fluorescent dye Atto532-maleimide with the residue Cys-208. After coupling, free Atto532-maleimide was removed using a size-exclusion column and by concentrating the labeled protein sample using a 10-kDa cutoff. Single-molecule fluorescence spectroscopy measurements were performed at room temperature using a home-built confocal microscope setup (1) and a Nd:YAG laser (532 nm, Coherent). Measurements were carried out in a buffer containing 25 mM Tris (pH 8.0), 125 mM NaCl, and 2 mM $MgCl_2$ at various integrin concentrations (no integrin; 12, 60, 120, 240, and 556 nM integrin; 1.12, 2.45, and 4.9 μM integrin). Mean diffusion times (τ_D) through the confocal detection volume of ∼7 fl were measured by fluorescence correlation spectroscopy by recording the autocorrelation signal for 120 s. The percentage of complex formed was calculated based on the different correlation times of pb9 (1.05 ms) and the pb9s–$\alpha_V\beta_3$ complex (1.63 ms). The K_D value was determined by plotting the percentage of complex formed in function of the added integrin concentration. Nonlinear regression analysis yielded a K_D of 415 ± 62 nM.

Negative-Stain EM Specimen Preparation. All samples were analyzed using C-flat 2/0.5 grids overlaid with a thin layer of carbon. Unliganded $\alpha_V\beta_3$ integrin or $\alpha_V\beta_3$ in complex with pb9 were diluted to 0.006 and 0.004 mg/mL with a buffer containing 10 mM Tris (pH 7.5), 150 mM NaCl, and 2 mM $MnCl_2$. Approximately 3–4 μL of sample were applied to glow-discharged grids before washing with deionized water and staining with 2% (wt/vol) uranyl-formate.

EM Data Collection and Processing. Data were collected using either an FEI Tecnai F20 Twin transmission electron microscope operated at 120 kV and equipped with a 4k × 4k Gatan US4000 camera (unliganded $\alpha_V\beta_3$) or an FEI Tecnai 12 transmission electron microscope operated at 120 kV and equipped with a 4k × 4k TVIPS F416 camera ($\alpha_V\beta_3$ in complex with pb9). A total of 270 image pairs (0° and −50°) were collected for the unliganded $\alpha_V\beta_3$ using a defocus range comprised between 0.1 and 2.55 μm and a total exposure of 32 e/Å^2 (the pixel size at the specimen level was 1.75 Å). A total of 802 image pairs (0° and 55°) were collected for $\alpha_V\beta_3$ in complex with pb9 using a defocus range comprised between 0.1 and 2.8 μm with a total exposure of 23 e/Å^2 (the pixel size at the specimen level was 2.05 Å). Data acquisition was automated using the Leginon software (2, 3), and data processing was carried out using the Appion pipeline (4, 5), which interfaces with the Leginon database infrastructure. The contrast transfer function (CTF) was estimated for each micrograph using CTFFIND3 (6), and particles were automatically selected from the micrographs using the template-based particle picker FindEM (7). Subsequently, particle images were extracted using a box size of 256 pixels (decimated by a factor of 2), and CTF correction was performed by phase flipping using EMAN 1.9 (8). A filtering strategy for removing outlying particles was conducted using Xmipp reference-free maximum-likelihood alignment and clustering (9) yielding 11,817 (unliganded $\alpha_V\beta_3$) and 28,168 ($\alpha_V\beta_3$ in complex with pb9) untilted particle images. The resulting reference-free class averages were used to align the particle images using Spider (10) before running several iterations of the Sparx iterative stable alignment and clustering software (ISAC) (11). Well-defined and unique class averages generated by ISAC were used as references for iterative alignment using Spider and classification using Imagic multivariate statistical analysis (12). Particle images were clustered in 15 (unliganded $\alpha_V\beta_3$) and 40 ($\alpha_V\beta_3$ in complex with pb9) different class averages, and random conical tilt reconstructions (13) were computed for all of them using the initial model pipeline within the Appion architecture. The resolution of the different reconstructions is estimated to be ∼50–60 Å according to the Fourier shell correlation criterion at 0.5. All reconstructions were low-pass filtered at a 30-Å resolution. Fitting of the atomic models within the reconstructions was achieved using University of California at San Francisco Chimera (14) and Coot (15).

1. Börsch M, Diez M, Zimmermann B, Reuter R, Gräber P (2002) Stepwise rotation of the gamma-subunit of EF(0)F(1)-ATP synthase observed by intramolecular single-molecule fluorescence resonance energy transfer. *FEBS Lett* 527(1-3):147–152.
2. Suloway C, et al. (2005) Automated molecular microscopy: The new Leginon system. *J Struct Biol* 151(1):41–60.
3. Yoshioka C, et al. (2007) Automation of random conical tilt and orthogonal tilt data collection using feature-based correlation. *J Struct Biol* 159(3):335–346.
4. Lander GC, et al. (2009) Appion: An integrated, database-driven pipeline to facilitate EM image processing. *J Struct Biol* 166(1):95–102.
5. Voss NR, Yoshioka CK, Radermacher M, Potter CS, Carragher B (2009) DoG Picker and TiltPicker: Software tools to facilitate particle selection in single particle electron microscopy. *J Struct Biol* 166(2):205–213.
6. Mindell JA, Grigorieff N (2003) Accurate determination of local defocus and specimen tilt in electron microscopy. *J Struct Biol* 142(3):334–347.
7. Roseman AM (2004) FindEM: A fast, efficient program for automatic selection of particles from electron micrographs. *J Struct Biol* 145(1-2):91–99.
8. Ludtke SJ, Baldwin PR, Chiu W (1999) EMAN: Semiautomated software for high-resolution single-particle reconstructions. *J Struct Biol* 128(1):82–97.

9. Scheres SH, et al. (2005) Maximum-likelihood multi-reference refinement for electron microscopy images. *J Mol Biol* 348(1):139–149.
10. Shaikh TR, et al. (2008) SPIDER image processing for single-particle reconstruction of biological macromolecules from electron micrographs. *Nat Protoc* 3(12):1941–1974.
11. Yang Z, Fang J, Chittuluru J, Asturias FJ, Penczek PA (2012) Iterative stable alignment and clustering of 2D transmission electron microscope images. *Structure* 20(2):237–247.
12. van Heel M, Harauz G, Orlova EV, Schmidt R, Schatz M (1996) A new generation of the IMAGIC image processing system. *J Struct Biol* 116(1):17–24.
13. Radermacher M (1988) Three-dimensional reconstruction of single particles from random and nonrandom tilt series. *J Electron Microsc Tech* 9(4):359–394.
14. Pettersen EF, et al. (2004) UCSF Chimera: A visualization system for exploratory research and analysis. *J Comput Chem* 25(13):1605–1612.
15. Emsley P, Lohkamp B, Scott WG, Cowtan K (2010) Features and development of Coot. *Acta Crystallogr D Biol Crystallogr* 66(Pt 4):486–501.

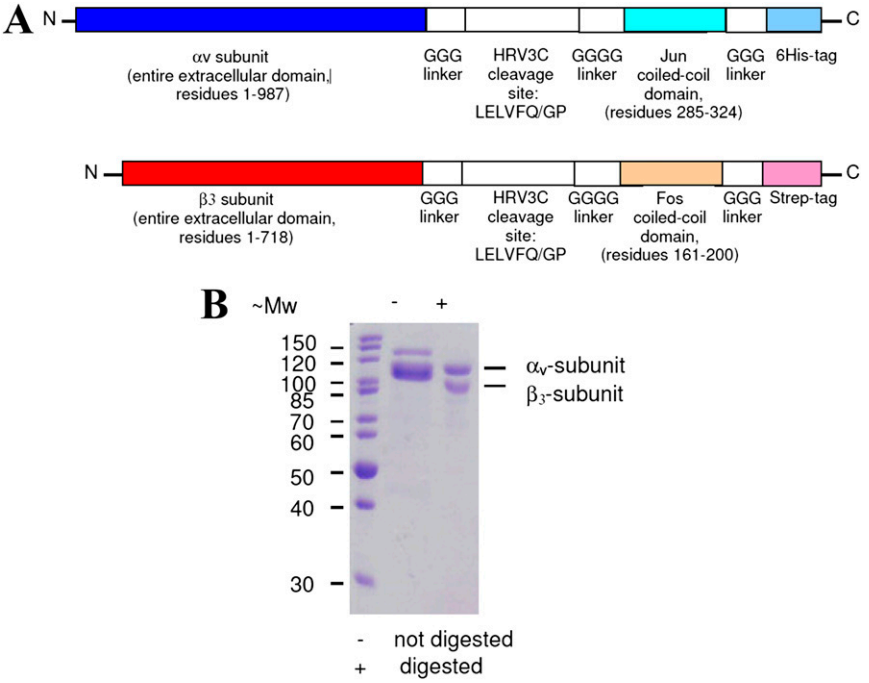

Fig. S1. Expression and purification of $\alpha_V\beta_3$ integrin. (*A*) Constructs used to overexpress the $\alpha_V\beta_3$ heterodimer. (*B*) SDS/PAGE of the overexpressed and purified $\alpha_V\beta_3$ heterodimer.

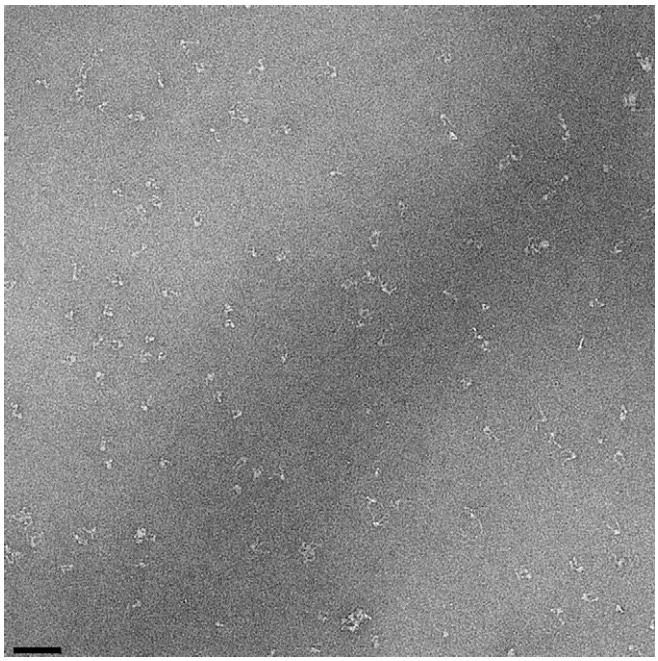

Fig. S2. Raw electron micrograph of isolated $\alpha_V\beta_3$ integrin. (Scale bar: 525 Å.)

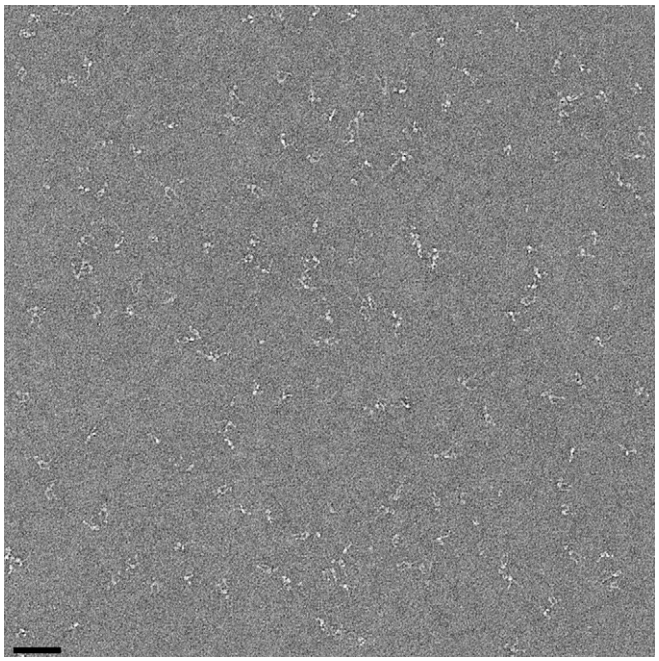

Fig. S3. Raw electron micrograph of the $\alpha_V\beta_3$ integrin–pb9 complex. (Scale bar: 615 Å.)

Movie S1. Conformational flexibility of $\alpha_V\beta_3$ integrin. Movie showing various snapshots of the extended integrin heterodimer observed in the 2D class averages obtained in this study.

Movie S1

Movie S2. Plasticity of interactions between pb9 and $\alpha_V\beta_3$ integrin. Various snapshots of the extended integrin heterodimer in combination with the distinct pb9-binding modes observed in the 2D class averages obtained in this study are shown.

Movie S2